

Precision cosmology with time delay lenses: high resolution imaging requirements

Xiao-Lei Meng,¹ Tommaso Treu,^{1,2} Adriano Agnello,^{1,2} Matthew W. Auger,³ Kai Liao,^{1,2} Philip J. Marshall⁴

¹Department of Physics, University of California, Santa Barbara, CA 93106, USA

²Physics and Astronomy Building, 430 Portola Plaza, Box 951547, Los Angeles, CA 90095-1547, USA

³Institute of Astronomy, University of Cambridge, Madingley Road, Cambridge CB3 0HA, UK

⁴Kavli Institute for Particle Astrophysics and Cosmology, Stanford University, 452 Lomita Mall, Stanford, CA 94305, USA

E-mail: xlmeng919@gmail.com

Abstract. Lens time delays are a powerful probe of cosmology, provided that the gravitational potential of the main deflector can be modeled with sufficient precision. Recent work has shown that this can be achieved by detailed modeling of the host galaxies of lensed quasars. The distortion of the images as measured over large number of pixels provides tight constraints on the difference between the gravitational potential between the quasar image positions, and thus on cosmology in combination with the measured time delay. We carry out a systematic exploration of the high resolution imaging required to exploit the thousands of lensed quasars that will be discovered by current and upcoming surveys with the next decade. Specifically we simulate realistic lens systems as imaged by the Hubble Space Telescope (HST), James Webb Space Telescope (JWST), ground based adaptive optics images taken with Keck or the Thirty Meter Telescope (TMT). We compare the performance of these pointed observations with that of images taken by the Euclid-VIS, Wide-Field Infrared Survey Telescope (WFIRST) and Large Synoptic Survey Telescope (LSST) surveys. We use as our metric the precision with which the slope γ' of the total mass density profile $\rho_{tot} \propto r^{-\gamma'}$ for the main deflector can be measured. Ideally, we require that the statistical error on γ' be less than 0.02, thus being subdominant with respect to other sources of random and systematic uncertainties. We find that survey data will likely have sufficient depth and resolution to meet the target only for the brighter gravitational lens systems, comparable to those discovered by the SDSS survey. For fainter systems, that will be discovered by current and future surveys, targeted follow-up will be required. However, the exposure time per target will be of order a few minutes per system with upcoming facilities, such as JWST, the Keck Next Generation Adaptive Optics System, and TMT, thus making the follow-up of hundreds of systems a practical and efficient cosmological probe.

Contents

1	Introduction	1
2	Summary of simulated instrumental setups	3
3	The Lens Sample	4
3.1	Parameters of the Sample of Mock Lenses	4
4	Description of the inference process	5
4.1	Image generating process	6
4.1.1	Light Model	6
4.1.2	Mass Model	6
4.1.3	Point Source Model	7
4.1.4	Image Noise	7
5	Inferring the parameters	7
6	Results	8
7	Summary	9

1 Introduction

In the past few years, gravitational time delays (Refsdal 1964 [1]) have emerged as a powerful and cost effective cosmological probe. Studies based on blind analysis have shown that a single system consisting of multiple images of a background quasar (at redshift z_s) lensed by a foreground massive elliptical galaxy at redshift z_d can be used to measure the so-called time delay distance with an uncertainty of 6-7% (Suyu et al. 2010 [2]; 2013 [3]; 2014 [4]). The time delay distance $D_{\Delta t}$ gives a direct measurement of the Hubble constant and allows one to break some the main degeneracies in the interpretation of cosmic microwave background data, thus providing tight constraints on parameters such as curvature and dark energy equation of state (Coe & Moustakas 2009 [5]; Linder 2011 [6]; Weinberg 2013 [7]; Suyu++12,Suyu++14). The time delay distance measurement of H_0 is comparable in terms of information content to that obtained via the cosmic distance ladder [? ?], in that is based on absolute distances and completely independent on the properties of the universe at $z > z_s$. Importantly, time delay distances are independent of the local distance ladder and thus provide a crucial test of any potential systematic uncertainties. Furthermore, being independent, the cosmic distance ladder and time delay distance constraints on H_0 can be statistically combined for additional gains in precision.

From an observational point of view, the attainment of precise and accurate time delay measurements relies on a few important ingredients. First, monitoring of the lensed quasars is required to obtain time delays with a few percent uncertainties. Dedicated monitoring campaigns have shown that this precision is achievable with 1-2m class telescopes at present time [?], or in the radio [?]. In the future, the exploitation of larger samples of lenses will require monitoring campaigns on 2-4m telescopes [?], or the deployment of long term high-cadence monitoring surveys, like the LSST [?]. Second, the spectroscopic redshift of the source and deflector must be measured . For current

samples, this is typically a relatively straightforward step, requiring short exposures on 4-10m class telescopes [? ?]. Third, the gravitational potential of the main deflector needs to be constrained by the data so that the uncertainty on its difference between the location of the images is also of order 3%. This goal can be achieved by studying the extended structure of the lensed quasar host galaxy, and the stellar kinematics of the deflector galaxy [? ? ? ? ?]. Fourth, the combined effects of the inhomogenous mass distribution along the line of sight need to be taken into account. Recent work has shown that the line of sight effects can be sufficiently characterized by measuring the properties of galaxies and weak lensing signal in the field of the main deflector, and comparing with simulated lines of sight (Suyu++10,++13,++14, Greene++13,Collet++13).

However, whereas current samples have been limited to a few lenses, current and ongoing surveys (add references to DES, PANSTARRS, HSC, ATLAS) will discover 100s of lenses. These large samples will be extremely powerful cosmographic probes [? ?], provided that sufficient follow-up data will be available [?]. In this paper we carry out a feasibility study for future time delay surveys, focusing on the high-resolution imaging requirements. Specifically, we aim to investigate whether sufficient information will be available from survey data, or whether dedicated follow-up will be necessary. If dedicated follow-up will be necessary, we aim to provide an estimate of the amount of time that will be required per system. The multi-pronged nature of time delay lens follow-up makes it natural to follow the approach of addressing each component of the follow-up independently. The monitoring and spectroscopic follow-up requirements are described, e.g., by [? ?].

In order to make the problem tractable and the results general, we need a single simple metric to evaluate the quality of imaging data. In short, we need to quantify our ability to measure how the deflection angle (i.e. the derivative of the lensing potential) varies between the images, and thus how the extended images of the quasar host galaxy are stretched across the image. In practice, our ability to constrain the differential magnification will depend on the resolution of the data as well as on the number of pixels where the source is detected (hereafter *informative pixels*).

We choose to adopt as our metric the slope γ' of the total mass density profile of the form $\rho_{\text{tot}} \propto r^{-\gamma'}$ as measured by fitting elliptical power law models to the data. This profile is the simplest one that provides a realistic description of galaxy scale lenses [?], and the uncertainty γ' has been shown to be approximately proportional to the uncertainty on the gravitational potential differences and thus the time delay distance [8–10]. Intuitively, γ' is directly related to the variations of the lensing potential. In fact, if $\gamma' = 2$ (the so-called isothermal profile) the deflection angle is constant across the image and therefore all the images will appear to have the same radial magnification. If the profile is steeper/shallower, radial magnification will vary across the image, thus giving rise to images of different widths.

Naturally, for a real measurement it is important to explore different profiles and the role of the choice of the profile in the uncertainties. However, our goal is to estimate minimal requirements on the data quality. If the data quality is insufficient to constrain γ' it will also be insufficient to constrain more flexible models. Likewise, systematic errors not considered in this paper, such as those arising from incomplete knowledge of the PSF, will only increase the error budget. Thus, in order to leave room for additional sources of uncertainty in the error budget, we set a rather stringent requirement of 0.02 uncertainty of γ' (corresponding approximately to 2% per system on time delay distance). In other words, our target corresponds to the requirement that the *statistical* error arising from the image quality be subdominant with respect to those arising from modeling uncertainties, time delays, and line of sight effects.

This paper is organized as follows. In Section 2, we summarize the characteristics of the telescopes and instruments simulated as part of this work. Then, in Section 3, we describe the properties of the simulated lenses. Next, in Section 4 we describe the procedure used to carry out the inference.

Our results are presented in Section 5. Finally, we discuss and summarize our work in Section 6. Throughout this paper, all magnitudes are given in the AB system. Even though our findings are independent of any cosmology, we adopt a spatially flat Λ CDM cosmology with $\Omega_m = 0.3$, $\Omega_\Lambda = 0.7$, and the Hubble constant $H_0 = 70 \text{ km s}^{-1} \text{ Mpc}^{-1}$ when calculating distances.

2 Summary of simulated instrumental setups

We aim to carry out a systematic exploration of imaging requirements given current and future facilities. For a given lens system, the instrumental setup drives our ability to constrain γ' in a number of ways. First, the signal-to-noise ratio depends on the exposure-time adopted, sky or background noise in a chosen band, and the instrumental readout noise. Second, the pixel-size and the point-spread function (PSF) properties determine how finely one can map the system being observed, hence how robustly the deflections on either side of the lens can be quantified.

Here we summarize the main properties of instruments that will be considered in our simulations. In an effort to balance completeness with feasibility, we consider a suite of instruments that include ground and space based telescopes, and cadenced surveys where the total exposure cannot be set arbitrarily. Some of the choices are representative of a class of telescopes/instruments, for example we expect the performance of Keck Adaptive Optics to be a useful guidance for adaptive optics systems on other 8-10m class telescopes, and that of the Thirty Meter Telescope to be a guidance for other planned 20-30m class telescopes.

Table 1 and figure 1 display the main properties of the telescopes that are needed when generating images of mock gravitational lenses, taken from the instrument websites. Figure 2 shows the typical PSF of each instrument. In order to facilitate comparisons between instruments and telescopes, whenever possible we selected the filter/band for each configuration that is closer to the I -band in the optical and the K' -band in the near infrared. A brief description of each setup follows.

1. The Advanced Camera for Surveys (ACS) is chosen as our reference optical imager on board the Hubble Space Telescope (HST). In the chosen F814W filter its performance is comparable to those of WFC3 (slightly higher sensitivity and coarser pixel size). For simplicity, we neglect charge transfer inefficiency effects, assuming that they are negligible or can be corrected to the desired level. The PSF is simulated using the Tiny Tim software (reference)
2. The Near Infrared Camera (NIRCAM) on board the James Webb Space Telescope (JWST) is chosen as the next space based imaging capability. We select the broad F200W filter, where the image quality is virtually diffraction limited.
3. The current and planned adaptive optics systems [hereafter LGSAO & NGAO [11](#), [12](#), respectively] at the W.M.Keck Observatory are chosen to represent current and upcoming AO performance on 8-10m class telescopes. We consider the current instrument NIRC2, although further gains might be possible with an instrument upgrade in conjunction with the AO system upgrade. We adopt the typical configuration used for studies of gravitational lens systems [[?](#)]: K' filter, MCDS readout mode, read number $N = 16$, and narrow camera mode. A real observed PSF is used for the current AO system. The simulated PSF and performance characteristics of NGAO have been kindly provided by the NGAO team.
4. The infrared imager and spectrograph IRIS [\[13\]](#) working behind adaptive optics on the thirty Meter Telescope is selected to represent the performance of the extremely large telescopes that will be operational in the next decade. TMT. IRIS is expected to be close to diffraction limited

in the K' band. The simulated PSF and performance characteristics of TMT-IRIS have been obtained from the IRIS team, from the TMT ETC¹ and from the paper by Do et al. (2014) [14].

5. Euclid is a space survey telescope planned to be launched by the European Space Agency. Euclid has two instruments: a high-resolution visible imager, and a NIR imaging instrument. We study the performance of the high-resolution visible imager, the more suitable to detailed gravitational lensing work, with the standard survey parameters. The instrument properties are taken from Schweitzer et al. 2010 [15], Penny et al. 2013 [16] and Cropper et al. 2014 [17]. Since the PSF is proprietary to the Euclid team, we adopt for simplicity a Gaussian function with full width half maximum $0.^{\prime}18$.
6. We study the survey mode of the 2.4m WFIRST space mission, focusing on the HLS Imaging Survey in the F184W filter. The instrument/survey properties are based on WFIRST-Astrophysics Focused Telescope Assets Final Report (by the Science Definition Team (ADT) and WFIRST Project) and WFIRST Exposure Time Calculator². Since the final PSF was not available at the time of this writing we adopt a Gaussian function with FWHM $0.^{\prime}15$.
7. The Large Synoptic Survey Telescope is designed to imaging surveys in the optical bands (out to ~ 1 micron). The survey and instrument properties are taken from Ivezic et al. 2008 (REFERENCE) and the LSST Science Requirements Document³. The PSF of LSST will vary over time. We adopt a Gaussian PSF with FWHM $0.^{\prime}7$ as representative of the image quality of LSST in the i-band.

3 The Lens Sample

Here we introduce our sample, four groups of lens system with galaxies at redshift $z_s = 1.071$ and 2.77 being multiply imaged by massive lens galaxies lying at $z_d = 0.351$ and 0.783 .

We have chosen four prototypical systems for this exploration, characterized as **faint** or **bright** and **double** or **quad** depending on the photometry and image configuration. This set of four main choices covers regimes with different numbers of informative pixels, which depend on the S/N ratio and on the number of images produced by the lens.

To remain as realistic as possible, the mocks are based upon lenses in the Sloan Lens ACS Survey (SLACS; Bolton et al. 2006 [18]; Treu et al. 2006 [19]; Koopmans et al. 2006 [20]; Gavazzi et al. 2007 [21]; Bolton et al. 2008a [22]; Gavazzi et al. 2008 [23]; Bolton et al. 2008b [24]; Treu et al. 2009 [25]; Auger et al. 2009 [26]; Auger et al. 2010 [27]; Newton et al. 2011 [28]; Shu et al. 2015 [29]; Papers I-XII, respectively) and the Strong Lensing Legacy Survey (SL2S; More et al. 2012 [30]; Gavazzi et al. 2012 ApJ...761..170G; Ruff et al. 2011 [31]; Sonnenfeld et al. 2013 [32]; Sonnenfeld et al. 2013 [33]; Sonnenfeld et al. 2015 [34]; Papers I-V, respectively, except for the first citation) samples.

3.1 Parameters of the Sample of Mock Lenses

The structural parameters of the four systems are listed in Table 2. When not explicitly known from existing data, mock model parameters are assigned via plausibility arguments as specified below. The source and deflector of the *bright* lens system configurations are built along SLACS J0330-0020 as

¹http://tmt.mtk.nao.ac.jp/ETC_readme.html

²<http://wfirst-web.ipac.caltech.edu/wfDepc/wfDepc.jsp?etc>

³<http://www.lsst.org/files/docs/SRD.pdf>

modelled by Bolton et al. 2008a (SLACS V, [22]), Auger et al. 2009 (SLACS IX, [26]), and Newton et al. 2011 (SLACS XI, [28]). For the *faint* lens system configuration, the source and deflector have parameters from the Sonnenfeld et al. 2013 (SL2S III, [32]) model of SL2S J135949+553550 and the discussion with Sonnenfeld. Source and deflector magnitudes in the *bright* case for I and V bands are from Newton et al. 2011 ([28]), for K band are estimated based on the other colors, and typical spectral energy distributions (i.e. an early-type galaxy for the deflector and a star forming galaxy for the source). Meanwhile, source magnitudes in the *faint* case are arbitrarily set to 25.0 in all bands.

Deflector magnitudes in the *faint* case are not directly available from the data, so they require some extrapolations. The value for I band is based on Sonnenfeld et al. 2013 (SL2S III, [32]), while for K and VIS bands are estimated according to their wavelength, assuming typical spectral energy distributions. Unknown magnitudes in *K* band are assigned from *H*-band ones via $K_{AB} = H_{AB}$. In addition, the effective (half-light) radius which are fitted in *bright* systems are evaluated in different bands for getting a precise estimate of the effective radius and its uncertainties. Differently, a unique effective radius is asserted across bandpasses for the *faint* systems. That means color gradient in photometric information is ignored for simplicity as this approximation does not affect the ability to recover the masss density profile in any significant way [32].

For both the faint and the bright systems, the source positions are assigned so as to map the source in either two or four images. This choice allows us to explore whether the number of images makes any substantial difference while keeping the other properties of the systems fixed.

In order to construct realistic systems for time delay measurements, we need to add point sources to represent the lensed quasars. As described in the next section this is done in the image plane, in order to gain computational precision and efficiency. The magnification at the location of the quasar images is calculated by solving the lens equation using `gravlens` [35]. The source-plane magnitudes of the point sources are chosen to be somewhat brighter then the host galaxy, as it is typically the case for medium luminosity AGN [e.g., ?], and have realistic colors for AGN at the source redshifts. The adopted magnitudes are listed in Table 4. We note that the bright source configuration is too bright to be practical for TMT, given its sensitivity (the exposure time scales as D^{-4} , where D is the telescope diameter, for background limited point source exposures). Realistically, observations of such bright systems would be completely dominated by overheads related to target acquisition and will only be carried out in extremely rare circumstances. Therefore we do not simulate TMT observations for the bright systems. Even for the fainter system, we have chosen to make the source galaxies artificially fainter ($K=26$) in order to avoid saturating the central pixels while imaging deep enough to get a sufficient signal to noise ratio on the host galaxy. As will be shown below, the exposure time requirements for TMT are extremely short even in these cases.

4 Description of the inference process

In this section, we briefly present the progress of modeling the mock lens systems using defined models. By comparing the distribution of the ratio between the inferred values and the input, we obtain the desired estimate of the statistical precision with which each parameter can be determined. As motivated in the introduction, we are interested primarily in the mass density profile slope γ' . Therefore, we will only show the statistics for that parameter, even though all the parameters are varied simultaneously during the inference. We first describe the image generating process in Section 4.1, and then we describe the inference process in Section ??.

4.1 Image generating process

Before we fit the mock lens system we need to define the models to describe the source galaxy light, the lens galaxy light, and the lens mass. We start with the surface brightness distribution of the galaxies. To remap the source image onto the source plane, the mass model for the lens mass distribution is needed to build to represent the deflection angle. Similarly, we also need a model for the light distribution of the lens galaxy. A PSF is used to convolve the light of lens galaxy, lensed source galaxy and point-source. Finally, we introduce three terms to describe the noise adding to the image, including counts noise, readout noise, and background noise. These steps are described in this section.

4.1.1 Light Model

We use the Sérsic profile [36, 37] to describe the surface brightness distribution of both the source and the deflector. The Sérsic profile is described by the equation [38]:

$$I(R) = I_e \exp \left[-k \left(\left(\frac{R}{R_{\text{eff}}} \right)^{\frac{1}{n}} - 1 \right) \right], \quad (4.1)$$

$$R(x, y, q) = \sqrt{qx^2 + y^2/q}. \quad (4.2)$$

The amplitude I_e is the intensity at the effective radius R_{eff} , the constant k is determined so that R_{eff} is the half light radius [?], the Sérsic index n controls the degree of curvature of the radial light profile, the $\{x, y\}$ represents the galaxy positions, and q denotes the axis ratio. Empirically, n increases with galaxy luminosity, most galaxies being fitted by Sérsic index in the range $0.6 \leq n \leq 10.0$ [39]. We adopt $n = 4$ for the deflectors (typical of massive early-type galaxies) and $n = 4/3$ or $n = 4$ for the sources, consistent with typical observed values for blue galaxies and AGN hosts. We checked by re-running simulations with different n for the source that our results do not depend significantly by this model assumption **XLM to do**.

4.1.2 Mass Model

Here we describe the distribution of the surface mass density for the lens galaxy. The deflector's mass profile is assigned within a class of power-law models,

$$\Sigma(x, y) = \Sigma_0 (qX^2 + q^{-1}Y^2)^{-\gamma'/2}, \quad (4.3)$$

where q is the axis ratio, γ' represents the radial power-law slope, the $\{X, Y\}$ axes are rotated by the lens position angle w.r.to the canonical x (increasing to the West) and y (increasing to the North). This means that the $\{X, Y\}$ deflections scale as ..., where $g(\theta)$ a just function of the relative angle west-of-north. Fast methods to compute deflections from power-law profiles have been given by Barkana 1998 [40]. Power-law models of elliptical galaxies (Evans 1994 [41]) have often been used with success over the years to model gravitational lenses. In all generality, the lensing deflections are given by

$$\alpha(\theta) = \frac{2}{\theta} \int_0^\theta \theta d\theta \Sigma(\theta) / \Sigma_{\text{cr}} \quad (4.4)$$

where θ is the position angle, and

$$\Sigma_{\text{cr}} = \frac{c^2 D_s}{4\pi G D_d D_{ds}} \quad (4.5)$$

encompasses the relative positions of source, deflector and observer (the angular diameter to the deflector (D_d), to the source (D_s), and between the deflector and the source (D_{ds})). Then, in our power-law case the deflections can be rewritten conveniently as

$$\alpha(\vartheta) = \theta_E \left(\frac{\theta_E}{\vartheta} \right)^{\gamma' - 2}, \quad (4.6)$$

$$(4.7)$$

where $\vartheta = R/D_d$, and R is the two-dimensional projected radius. θ_E here is the Einstein radius R_E , which is such that in the spherical case ($q = 1$) the mean dimensionless density $\langle \Sigma \rangle / \Sigma_{cr}$ within a circle of radius R_E is exactly 1. This is also the radius of a ring traced by the host of the quasar when this is exactly aligned with the lens galaxy.

Lensed image profiles are obtained by inverse ray shooting. First, each pixel position in the image plane is mapped back to the source plane via the deflections in Eq 4.6. Then, we exploit the fact that surface-brightness is preserved by lensing to assign surface brightness to each detector pixel in the image plane. Given the smoothly varying surface brightness distribution of the source host galaxy, a rectangular grid in the image-plane is adopted. As discussed in the next section, this approximation would be too crude to represent properly the sharp point source associated with the quasar images, which are therefore added directly to the image plane. Finally, the light models models are convolved with the PSF appropriate for each instrument.

4.1.3 Point Source Model

In order to reduce computation time and complexity, the point source images are added to the light model by adding a PSF with appropriate normalization and position directly to the image plane. The normalization and position of the images for the center of the source in the source plane are computed for each configuration by solving the lens equation using `gravlens` [35].

4.1.4 Image Noise

In the final step of our simulations we account for the effect of noise arising from the counts statistics, the background, and detector read out. As usual, the variance of noise per pixel is given by

$$\text{Var}_{\text{pix}} = \sqrt{Ct + B \cdot t + N_{\text{read}}R^2} \quad (4.8)$$

where C is the signal from clean lens system in electrons per second per pixel, t is the integration time in seconds, B_{sky} is the sum of the sky background and detector dark current in electrons per second per pixel, N_{read} is the number of detector readouts, and R is the standard deviation of the read noise in electrons. Realistically, when long integration times are required, we set the number of readouts by requiring no single exposure be longer than a maximum time that depends on each instrument configuration **XLM: what's tmax for the various instruments?**. Examples of simulated images are shown in Figure 3 to ??.

5 Inferring the parameters

The same code is used to generate the mock models and to fit them. The model fits the following parameters: **XLM to list all free parameters**. As usual the likelihood is assessed through the image-plane χ^2 , by comparing the model and mock data surface brightness profiles. Uncertainties are obtained via MCMC exploration of the likelihood, which in this case is simply given by $\mathcal{L} \propto \exp[-\chi^2/2]$.

The quasar images are not used in the inference, which is performed just on the lensed host. This is because, in practice, the point-like images of the quasar are time variable and usually appreciably affected by microlensing, milli-lensing and dust lanes in the foreground, and therefore provide a limited amount of useful information on the differences in gravitational potential. Our process is a faster version of the standard practice of removing the point images in the image plane before fitting the host galaxy [?]. By not fitting the point source position we speed up the inference significantly, while not giving up a large amount of information. Clearly, our approximation does not allow us to verify the impact of systematic uncertainties related to the reconstruction and subtraction of the PSF, which may in some cases be substantial. A full characterization of this source of uncertainty is beyond the scope of this paper and is left for future work.

The inference is computationally expensive: typical run times range between **X and Y seconds per system, XLM to specify** on a linux desktop computer.

6 Results

The goal of this work is to investigate what combinations of instrument/telescope configuration and exposure time produce images of quality sufficient to determine γ' with 2% precision.

For the telescopes/instruments operated in observatory mode, we are able to set the exposure time to any desired level. The minimum exposure time required is defined as the “target” exposure time. In addition, in order to quantify how the precision on γ' depends on exposure time, we also simulated images with $1/3$ and $3\times$ the exposure time. This is meant to provide useful guidance for designing future experiments. However, for some combination of lens brigtheness and telescope/instrument configratio, the target exposure time is too short to be adopted in realistic observations. In practice, therefore these lenses will either not be observed with this setup or be observed for longer exposure time. Taking into account typical overheads for pointing and acquisition we evaluated that the *brighter* lenses are too bright to be observed with TMT, while a minimum exposure time of 360s gives more than enough signal-to-noise ratio for the fainter systems. Likewise the brighter systmes are likely too bright to be observed with JWST. We still simulated them, but set the minimum exposure time to 60s.

For the telescopes/instruments to be operated in survey mode, we simulated the planned exposure time, and considered the specific question of whether the ensuing data quality is sufficient or not to meet the requirement.

Using the methods summarized in the previous section we generate 10 mock systems for each configuration, and carry out the full inference for each one using the python Markov Chain Monte Carlo sampler `pymc`. The results are summarized in Figures 7 to

First of all, we find that HST can deliver the desired image quality with exposures of a few ks at most, consistent with published work [?]. Conversely it seems that current AO capabilities, even setting aside the difficulties associated with the reconstruction of the PSF, are only sufficient to study the brighter systems with reasonable exposure times. The improvement with NGAO will be substantial, cutting integration times down to HST-like for both the bright and the faint lenses. In this case, the higher background than from space is compensated by the advantage of having smaller detector pixels, and thus better sampling of the PSF, and a larger telescope aperture.

For TMT we concluded that 360s of exposure will be more than sufficient for all systems considered here and therefore TMT is likely to be used either to take a brief image before taking a spectrum for determining the deflector velocity field and source redshift, or to follow-up fainter systems, yet to be discovered. Similary, JWST can obtain images of the desired quality in just a few minutes, and

therefore it is likely to be used mostly to take images before taking a spectrum or to follow-up fainter systems.

For the surveys, the conclusion is that while the Euclid survey seems to have insufficient depth and resolution to meet our requirements on the targets considered here, LSST and WFIRST should be sufficient at least for the brighter ones. Of course, these surveys will cover vast fractions of the sky and will therefore provide at no additional cost useful images for all the brighter systems. Those will be a great complement to the deeper pointed observation obtained with the other telescopes. WFIRST is planned to have a component of GO program, so it could meet the imaging requirements by integrating longer than in the survey mode. In fact, WFIRST is expected to have imaging performance superior to that of WFC3 on board HST, which has already been used to perform studies of time delay lenses, using integration times of a few orbits per system ($\sim 10\text{ks}$; HST-GO-12889, PI: Suyu).

7 Summary

Acknowledgments

AA, and TT acknowledge support from NSF grant AST-1450141 “Collaborative Research: Accurate cosmology with strong gravitational lens time delays”. AA, and TT gratefully acknowledge support by the Packard Foundation through a Packard Research Fellowship to TT. The work of PJM was supported by the U.S. Department of Energy under contract number DE-AC02-76SF00515.

[...]

References

- [1] S. Refsdal, *On the possibility of determining Hubble’s parameter and the masses of galaxies from the gravitational lens effect*, Mon. Not. R. Astron. Soc. **128** (1964) 307.
- [2] S. H. Suyu, P. J. Marshall, M. W. Auger, S. Hilbert, R. D. Blandford, L. V. E. Koopmans, C. D. Fassnacht, and T. Treu, *Dissecting the Gravitational lens B1608+656. II. Precision Measurements of the Hubble Constant, Spatial Curvature, and the Dark Energy Equation of State*, Astrophys. J. **711** (Mar., 2010) 201–221, [[arXiv:0910.2773](#)].
- [3] S. H. Suyu, M. W. Auger, S. Hilbert, P. J. Marshall, M. Tewes, T. Treu, C. D. Fassnacht, L. V. E. Koopmans, D. Sluse, R. D. Blandford, F. Courbin, and G. Meylan, *Two Accurate Time-delay Distances from Strong Lensing: Implications for Cosmology*, Astrophys. J. **766** (Apr., 2013) 70, [[arXiv:1208.6010](#)].
- [4] S. H. Suyu, T. Treu, S. Hilbert, A. Sonnenfeld, M. W. Auger, R. D. Blandford, T. Collett, F. Courbin, C. D. Fassnacht, L. V. E. Koopmans, P. J. Marshall, G. Meylan, C. Spinelli, and M. Tewes, *Cosmology from Gravitational Lens Time Delays and Planck Data*, Astrophys. J. **788** (June, 2014) L35, [[arXiv:1306.4732](#)].
- [5] D. Coe and L. A. Moustakas, *Cosmological Constraints from Gravitational Lens Time Delays*, Astrophys. J. **706** (Nov., 2009) 45–59, [[arXiv:0906.4108](#)].
- [6] E. V. Linder, *Lensing time delays and cosmological complementarity*, Phys. Rev. D **84** (Dec., 2011) 123529, [[arXiv:1109.2592](#)].
- [7] D. H. Weinberg, M. J. Mortonson, D. J. Eisenstein, C. Hirata, A. G. Riess, and E. Rozo, *Observational probes of cosmic acceleration*, Phys. Rept. **530** (Sept., 2013) 87–255, [[arXiv:1201.2434](#)].
- [8] C. S. Kochanek, *What Do Gravitational Lens Time Delays Measure?*, Astrophys. J. **578** (Oct., 2002) 25–32, [[astro-ph/0205319](#)].

- [9] O. Wucknitz, *Degeneracies and scaling relations in general power-law models for gravitational lenses*, Mon. Not. R. Astron. Soc. **332** (June, 2002) 951–961, [[astro-ph/0202376](#)].
- [10] S. H. Suyu, *Cosmography from two-image lens systems: overcoming the lens profile slope degeneracy*, Mon. Not. R. Astron. Soc. **426** (Oct., 2012) 868–879, [[arXiv:1202.0287](#)].
- [11] P. L. Wizinowich, D. Le Mignant, A. H. Bouchez, R. D. Campbell, J. C. Y. Chin, A. R. Contos, M. A. van Dam, S. K. Hartman, E. M. Johansson, R. E. Lafon, H. Lewis, P. J. Stomski, D. M. Summers, C. G. Brown, P. M. Danforth, C. E. Max, and D. M. Pennington, *The W. M. Keck Observatory Laser Guide Star Adaptive Optics System: Overview*, PASP **118** (Feb., 2006) 297–309.
- [12] P. Wizinowich, S. Adkins, R. Dekany, D. Gavel, C. Max, R. Bartos, J. Bell, A. Bouchez, J. Chin, A. Conrad, A. Delacroix, E. Johansson, R. Kupke, C. Lockwood, J. Lyke, F. Marchis, E. McGrath, D. Medeiros, M. Morris, D. Morrison, C. Neyman, S. Panteleev, M. Pollard, M. Reinig, T. Stalcup, S. Thomas, M. Troy, K. Tsubota, V. Velur, K. Wallace, and E. Wetherell, *W. M. Keck Observatory’s next-generation adaptive optics facility*, in *Society of Photo-Optical Instrumentation Engineers (SPIE) Conference Series*, vol. 7736 of *Society of Photo-Optical Instrumentation Engineers (SPIE) Conference Series*, p. 0, July, 2010.
- [13] J. E. Larkin, A. M. Moore, E. J. Barton, B. Bauman, K. Bui, J. Canfield, D. Crampton, A. Delacroix, M. Fletcher, D. Hale, D. Loop, C. Niehaus, A. C. Phillips, V. Reshetov, L. Simard, R. Smith, R. Suzuki, T. Usuda, and S. A. Wright, *The infrared imaging spectrograph (IRIS) for TMT: instrument overview*, in *Society of Photo-Optical Instrumentation Engineers (SPIE) Conference Series*, vol. 7735 of *Society of Photo-Optical Instrumentation Engineers (SPIE) Conference Series*, p. 29, July, 2010. [[arXiv:1007.1973](#)].
- [14] T. Do, S. A. Wright, A. J. Barth, E. J. Barton, L. Simard, J. E. Larkin, A. M. Moore, L. Wang, and B. Ellerbroek, *Prospects for Measuring Supermassive Black Hole Masses with Future Extremely Large Telescopes*, Astron. J. **147** (Apr., 2014) 93, [[arXiv:1401.7988](#)].
- [15] M. Schweitzer, R. Bender, R. Katterloher, F. Eisenhauer, R. Hofmann, R. Saglia, R. Holmes, O. Krause, H.-W. Rix, J. Booth, P. Fagrelius, J. Rhodes, S. Seshadri, A. Refregier, J. Amiaux, J.-L. Augueres, O. Boulade, C. Cara, A. Amara, S. Lilly, E. Atad-Ettedgui, A.-M. di Giorgio, L. Duvet, C. Kuehl, and M. Syed, *NIP: the near infrared imaging photometer for Euclid*, in *Society of Photo-Optical Instrumentation Engineers (SPIE) Conference Series*, vol. 7731 of *Society of Photo-Optical Instrumentation Engineers (SPIE) Conference Series*, p. 1, July, 2010.
- [16] M. T. Penny, E. Kerins, N. Rattenbury, J.-P. Beaulieu, A. C. Robin, S. Mao, V. Batista, S. Calchi Novati, A. Cassan, P. Fouqué, I. McDonald, J. B. Marquette, P. Tisserand, and M. R. Zapatero Osorio, *ExELS: an exoplanet legacy science proposal for the ESA Euclid mission - I. Cold exoplanets*, Mon. Not. R. Astron. Soc. **434** (Sept., 2013) 2–22, [[arXiv:1206.5296](#)].
- [17] M. Cropper, S. Pottinger, S.-M. Niemi, J. Denniston, R. Cole, M. Szafraniec, Y. Mellier, M. Berthé, J. Martignac, C. Cara, A. M. di Giorgio, A. Sciortino, S. Paltani, L. Genolet, J.-J. Fourmand, M. Charra, P. Guttridge, B. Winter, J. Endicott, A. Holland, J. Gow, N. Murray, D. Hall, J. Amiaux, R. Laureijs, G. Racca, J.-C. Salvignol, A. Short, J. Lorenzo Alvarez, T. Kitching, H. Hoekstra, and R. Massey, *VIS: the visible imager for Euclid*, in *Society of Photo-Optical Instrumentation Engineers (SPIE) Conference Series*, vol. 9143 of *Society of Photo-Optical Instrumentation Engineers (SPIE) Conference Series*, p. 0, Aug., 2014.
- [18] A. S. Bolton, S. Burles, L. V. E. Koopmans, T. Treu, and L. A. Moustakas, *The Sloan Lens ACS Survey. I. A Large Spectroscopically Selected Sample of Massive Early-Type Lens Galaxies*, Astrophys. J. **638** (Feb., 2006) 703–724, [[astro-ph/0511453](#)].
- [19] T. Treu, L. V. Koopmans, A. S. Bolton, S. Burles, and L. A. Moustakas, *The Sloan Lens ACS Survey. II. Stellar Populations and Internal Structure of Early-Type Lens Galaxies*, Astrophys. J. **640** (Apr., 2006) 662–672, [[astro-ph/0512044](#)].
- [20] L. V. E. Koopmans, T. Treu, A. S. Bolton, S. Burles, and L. A. Moustakas, *The Sloan Lens ACS Survey*.

III. The Structure and Formation of Early-Type Galaxies and Their Evolution since $z \sim 1$, *Astrophys. J.* **649** (Oct., 2006) 599–615, [[astro-ph/0601628](#)].

- [21] R. Gavazzi, T. Treu, J. D. Rhodes, L. V. E. Koopmans, A. S. Bolton, S. Burles, R. J. Massey, and L. A. Moustakas, *The Sloan Lens ACS Survey. IV. The Mass Density Profile of Early-Type Galaxies out to 100 Effective Radii*, *Astrophys. J.* **667** (Sept., 2007) 176–190, [[astro-ph/0701589](#)].
- [22] A. S. Bolton, S. Burles, L. V. E. Koopmans, T. Treu, R. Gavazzi, L. A. Moustakas, R. Wayth, and D. J. Schlegel, *The Sloan Lens ACS Survey. V. The Full ACS Strong-Lens Sample*, *Astrophys. J.* **682** (Aug., 2008) 964–984, [[arXiv:0805.1931](#)].
- [23] R. Gavazzi, T. Treu, L. V. E. Koopmans, A. S. Bolton, L. A. Moustakas, S. Burles, and P. J. Marshall, *The Sloan Lens ACS Survey. VI. Discovery and Analysis of a Double Einstein Ring*, *Astrophys. J.* **677** (Apr., 2008) 1046–1059, [[arXiv:0801.1555](#)].
- [24] A. S. Bolton, T. Treu, L. V. E. Koopmans, R. Gavazzi, L. A. Moustakas, S. Burles, D. J. Schlegel, and R. Wayth, *The Sloan Lens ACS Survey. VII. Elliptical Galaxy Scaling Laws from Direct Observational Mass Measurements*, *Astrophys. J.* **684** (Sept., 2008) 248–259, [[arXiv:0805.1932](#)].
- [25] T. Treu, R. Gavazzi, A. Gorecki, P. J. Marshall, L. V. E. Koopmans, A. S. Bolton, L. A. Moustakas, and S. Burles, *The SLACS Survey. VIII. The Relation between Environment and Internal Structure of Early-Type Galaxies*, *Astrophys. J.* **690** (Jan., 2009) 670–682, [[arXiv:0806.1056](#)].
- [26] M. W. Auger, T. Treu, A. S. Bolton, R. Gavazzi, L. V. E. Koopmans, P. J. Marshall, K. Bundy, and L. A. Moustakas, *The Sloan Lens ACS Survey. IX. Colors, Lensing, and Stellar Masses of Early-Type Galaxies*, *Astrophys. J.* **705** (Nov., 2009) 1099–1115, [[arXiv:0911.2471](#)].
- [27] M. W. Auger, T. Treu, A. S. Bolton, R. Gavazzi, L. V. E. Koopmans, P. J. Marshall, L. A. Moustakas, and S. Burles, *The Sloan Lens ACS Survey. X. Stellar, Dynamical, and Total Mass Correlations of Massive Early-type Galaxies*, *Astrophys. J.* **724** (Nov., 2010) 511–525, [[arXiv:1007.2880](#)].
- [28] E. R. Newton, P. J. Marshall, T. Treu, M. W. Auger, R. Gavazzi, A. S. Bolton, L. V. E. Koopmans, and L. A. Moustakas, *The Sloan Lens ACS Survey. XI. Beyond Hubble Resolution: Size, Luminosity, and Stellar Mass of Compact Lensed Galaxies at Intermediate Redshift*, *Astrophys. J.* **734** (June, 2011) 104, [[arXiv:1104.2608](#)].
- [29] Y. Shu, A. S. Bolton, J. R. Brownstein, A. D. Montero-Dorta, L. V. E. Koopmans, T. Treu, R. Gavazzi, M. W. Auger, O. Czoske, P. J. Marshall, and L. A. Moustakas, *The Sloan Lens ACS Survey. XII. Extending Strong Lensing to Lower Masses*, *ArXiv e-prints* (July, 2014) [[arXiv:1407.2240](#)].
- [30] A. More, R. Cabanac, S. More, C. Alard, M. Limousin, J.-P. Kneib, R. Gavazzi, and V. Motta, *The CFHTLS-Strong Lensing Legacy Survey (SL2S): Investigating the Group-scale Lenses with the SARCS Sample*, *Astrophys. J.* **749** (Apr., 2012) 38, [[arXiv:1109.1821](#)].
- [31] A. J. Ruff, R. Gavazzi, P. J. Marshall, T. Treu, M. W. Auger, and F. Brault, *The SL2S Galaxy-scale Lens Sample. II. Cosmic Evolution of Dark and Luminous Mass in Early-type Galaxies*, *Astrophys. J.* **727** (Feb., 2011) 96, [[arXiv:1008.3167](#)].
- [32] A. Sonnenfeld, R. Gavazzi, S. H. Suyu, T. Treu, and P. J. Marshall, *The SL2S Galaxy-scale Lens Sample. III. Lens Models, Surface Photometry, and Stellar Masses for the Final Sample*, *Astrophys. J.* **777** (Nov., 2013) 97, [[arXiv:1307.4764](#)].
- [33] A. Sonnenfeld, T. Treu, R. Gavazzi, S. H. Suyu, P. J. Marshall, M. W. Auger, and C. Nipoti, *The SL2S Galaxy-scale Lens Sample. IV. The Dependence of the Total Mass Density Profile of Early-type Galaxies on Redshift, Stellar Mass, and Size*, *Astrophys. J.* **777** (Nov., 2013) 98, [[arXiv:1307.4759](#)].
- [34] A. Sonnenfeld, T. Treu, P. J. Marshall, S. H. Suyu, R. Gavazzi, M. W. Auger, and C. Nipoti, *The SL2S Galaxy-scale Lens Sample. V. Dark Matter Halos and Stellar IMF of Massive Early-type Galaxies Out to Redshift 0.8*, *Astrophys. J.* **800** (Feb., 2015) 94, [[arXiv:1410.1881](#)].
- [35] C. R. Keeton, “GRAVELENS: Computational Methods for Gravitational Lensing.” *Astrophysics Source Code Library*, Feb., 2011.

- [36] J. L. Sérsic, *Influence of the atmospheric and instrumental dispersion on the brightness distribution in a galaxy*, *Boletin de la Asociacion Argentina de Astronomia La Plata Argentina* **6** (1963) 41.
- [37] J. L. Sérsic, *Atlas de galaxias australes*. 1968.
- [38] N. Caon, M. Capaccioli, and M. D’Onofrio, *On the Shape of the Light Profiles of Early Type Galaxies*, *Mon. Not. R. Astron. Soc.* **265** (Dec., 1993) 1013, [[astro-ph/9309013](#)].
- [39] D. Merritt, A. W. Graham, B. Moore, J. Diemand, and B. Terzić, *Empirical Models for Dark Matter Halos. I. Nonparametric Construction of Density Profiles and Comparison with Parametric Models*, *Astron. J.* **132** (Dec., 2006) 2685–2700, [[astro-ph/0509417](#)].
- [40] R. Barkana, *Fast Calculation of a Family of Elliptical Mass Gravitational Lens Models*, *Astrophys. J.* **502** (Aug., 1998) 531–537, [[astro-ph/9802002](#)].
- [41] N. W. Evans, *The power-law galaxies*, *Mon. Not. R. Astron. Soc.* **267** (Mar., 1994) 333–360.

Table 1. Telescope and Instrument Properties

Telescope	Instrument	Filter	Zero Point	Readout Noise (e ⁻ /pixel)	Background Noise (e ⁻ /pixel/s)	Pixel Size (arcsec)
HST	ACS	F814W	25.94	4.20	0.11	0.050
JWST	NIRCAM	F200W	27.85	9.00	0.20	0.032
LGSАО	NIRC2	<i>K'</i>	28.04	5.75	26	0.010
NGAO	NIRC2	<i>K'</i>	28.04	5.75	26	0.010
TMT	IRIS	<i>K'</i>	31.10	2.00	21	0.004
Euclid	VIS	<i>r + i + z</i>	25.58	4.50	0.43	0.100
WFIRST	DRM(?)	F184	26.18	5.00	0.11	0.110
LSST	—	<i>I</i>	28.35	5.00	68	0.200

Observational facilities (telescopes and instruments) considered in this work. Zero points are given in the ABmag system. The VIS imager of Euclid spans the whole *r + i + z* wavelength range. The Keck 10-m telescope is considered both with the current (LGSАО) and next-generation (NGAO) adaptive optics capabilities.

Table 2. Surface Brightness Profile Models

Lens Name	R_{eff} (arcsec)	q	P.A. (deg)	n	Δx (arcsec)	Δy (arcsec)	m_I	m_K	m_{VIS}	m_H
Parameters for the source										
fainter system ^a	0.23	0.92	54.0	4.0	0.0662	-0.167	25.0	25.0	25.0	25.0
fainter system ^b	0.23	0.92	54.0	4.0	0.008	0.298	25.0	25.0	25.0	25.0
brighter system ^b	0.12	0.77	120.0	1.33	-0.195	0.34	22.73	22.0	23.46	22.0
brighter system ^a	0.12	0.77	120.0	1.33	0.01	-0.005	22.73	22.0	23.46	22.0
Parameters for the deflector										
fainter system	1.76	0.61	-9.6	4.0	—	—	20.69	19.7	21.13	19.7
brighter system	0.91	0.81	113.2	4.0	—	—	17.99	16.5	18.84	16.5

R_{eff} is the half light radius. q denotes the axis ratio. P.A. is with respect to the x-axis. The Sérsic index n controls the degree of curvature of the galaxy light profile. Magnitudes m are given in the ABmag system. The only difference among systems with sources the same brightness is in the source-position, which is set to produce either two or four images of the center.

^a This configuration yields 4 QSO images.

^b This configuration yields 2 QSO images.

Table 3. Lens Model Parameters

Lens Name	z	R_{Ein} (arcsec)	q	P.A. (deg)	γ'
fainter system	0.783	1.14	0.6	14.7	2.0
brighter system	0.351	1.1	0.81	113.2	2.0

R_{Ein} is the Einstein radius, according to the definition by Kormann+94. q denotes the axis ratio of the mass distribution. P.A. is anti-clockwise from the x-axis. The model deflector is a Singular Isothermal Ellipsoid ($\gamma'=2$), which is then fit using power-law models with variable γ' .

Table 4. Point Source Parameters

	mag(I)	mag(K)	mag(VIS)	mag(H)	μ (I)	μ (II)	μ (III)	μ (IV)
fainter system ^a	24.0	24.0	24.0	24.0	2.84	3.75	6.59	2.78
fainter system ^b	24.0	24.0	24.0	24.0	2.78	2.48	—	—
brighter system ^b	21.7	21.5	22.9	21.5	1.22	6.10	—	—
brighter system ^a	21.7	21.5	22.9	21.5	6.09	8.22	6.86	7.53

Magnitudes (in the ABmag system) and magnifications of multiple images. The source magnitude ‘mag’ is given in the source plane so that the observed magnitude in the image plane is given by $\text{mag} - 2.5 \log_{10} \mu$, where μ is the magnification of each image.

^a This configuration yields 4 QSO images.

^b This configuration yields 2 QSO images.

Table 5. Exposure time requirements

Instrument	double		quad	
	faint	bright	faint	bright
HST	6×10^3 s	360 s	3×10^3 s	150 s
JWST	690s	360 s	210s	<60 s
Keck (LGSAO)	105×10^3 s	3600 s	75×10^3 s	2400 s
Keck (NGAO)	18×10^3 s	180 s	3×10^3 s	150 s

Exposure times required to attain a 2% precision on the inferred γ' . With 360 s of exposure, the TMT already enables percent-level precision. The Euclid, WFIRST and LSST surveys, are not quoted here because their exposure times are fixed. The default exposure times are sufficient to meet the 2% requirement in the case of LSST and WFIRST, but not for Euclid.

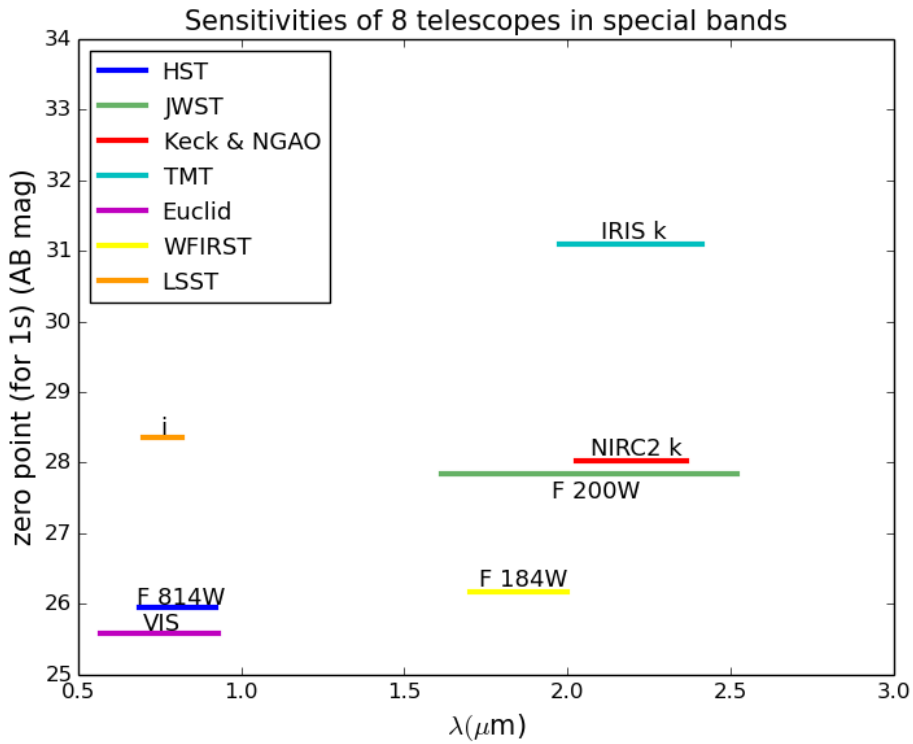


Figure 1. Zero points in AB magnitudes for HST/ACS (blue), JWST/NIRCAM (green), Keck NIRC2 (assumed for both LGSAs and NGAO; red), TMT/IRIS (cyan), Euclid (magenta), WFIRST (yellow) and LSST (orange), corresponding to one count per second. The colored bars indicate the wavelength range of each instrumental setup considered in this work.

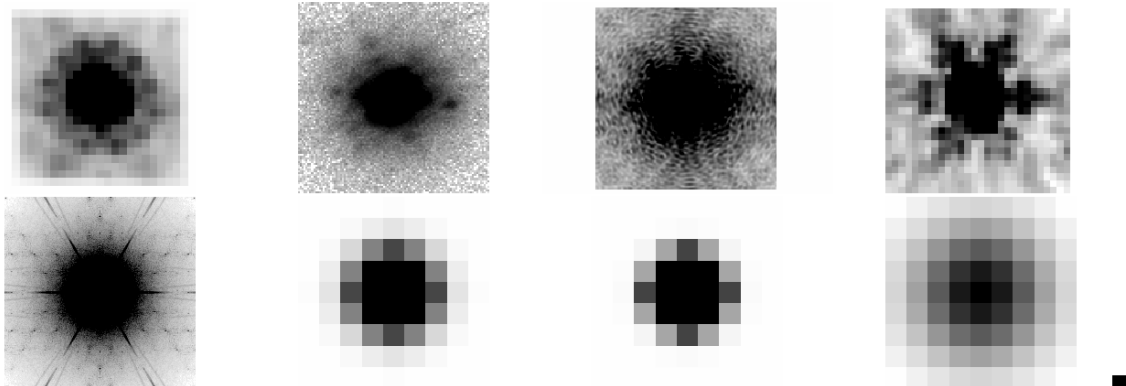


Figure 2. Montage of the point spread functions (PSFs) of each instrument. The upper row, from left to right, represents HST/ACS, Keck/NIRC2+LGSAs, Keck/NIRC2+NGAO, and JWST/NIRCAM. The lower row, from left to right, shows TMT/IRIS, Euclid, WFIRST, and LSST, respectively. Observed or simulated PSFs are used for HST, JWST, Keck (LGSAs & NGAO), and TMT. Gaussian PSFs are adopted for the other three survey instruments.

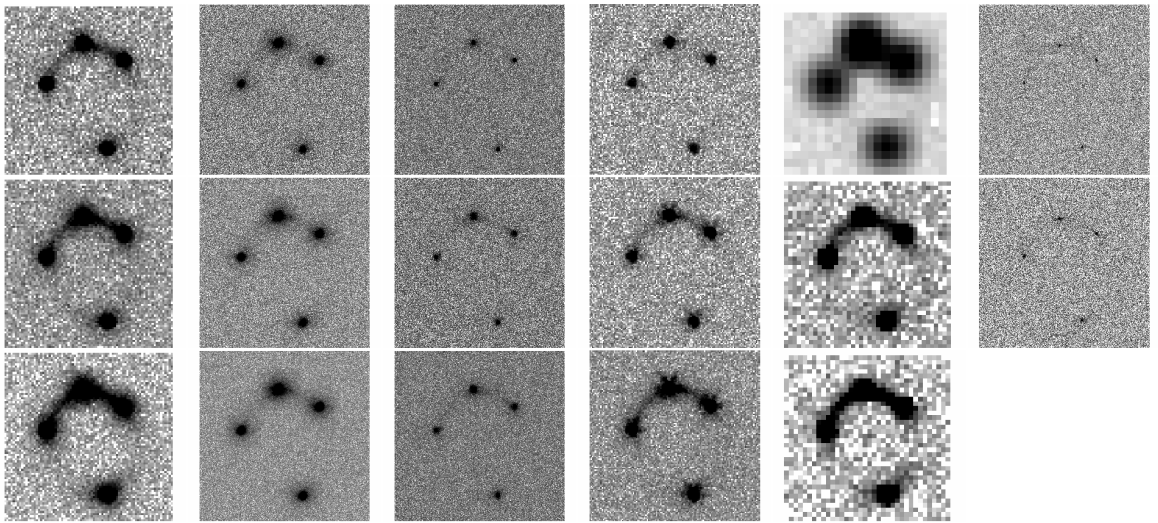


Figure 3. Simulations of the fainter lens system with 4 QSO images. The simulated images are all $4'' \times 4''$. The first 4 columns, from left to right, represent HST/ACS, Keck/NIRC2+LGS, Keck/NIRC2+NGAO, and JWST/NIRCAM; from top to bottom, the rows correspond to $1/3 \times$ “target” exposure time, “target” exposure time, and $3 \times$ “target” exposure time. “Target” exposure time is defined as the exposure time that yields 2% precision on the slope of the mass density profile of the mass model γ' . The fifth column shows simulations of 3 surveys. From top to bottom we show LSST, Euclid, and WFIRST, with the default survey exposure times (4500s, 2360s, 920s, respectively). The last column shows simulations for TMT with 2 fixed exposure times of 360 seconds and 1080 seconds.

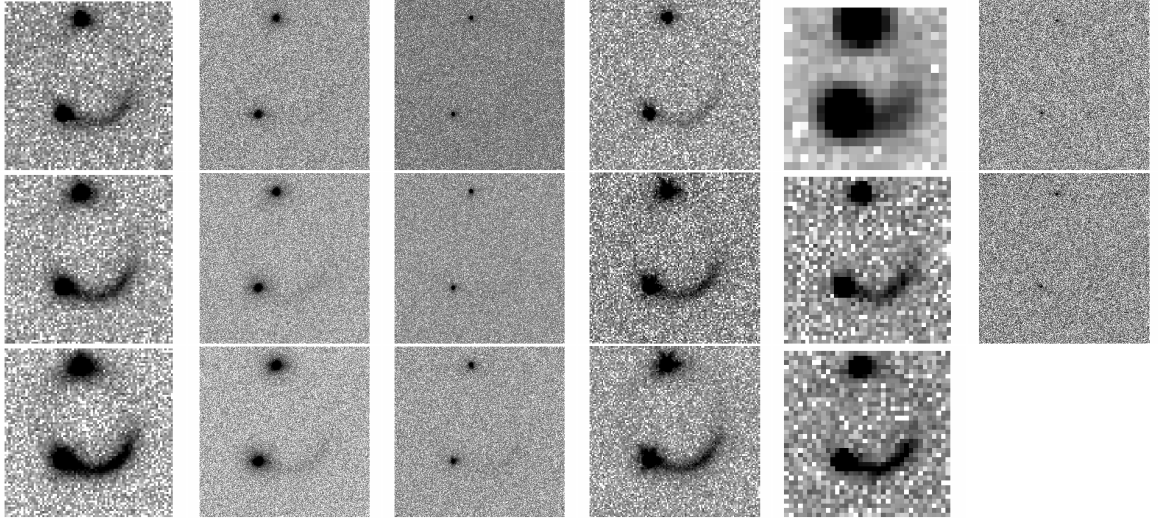


Figure 4. Same as Fig. 2, for the faint double system.

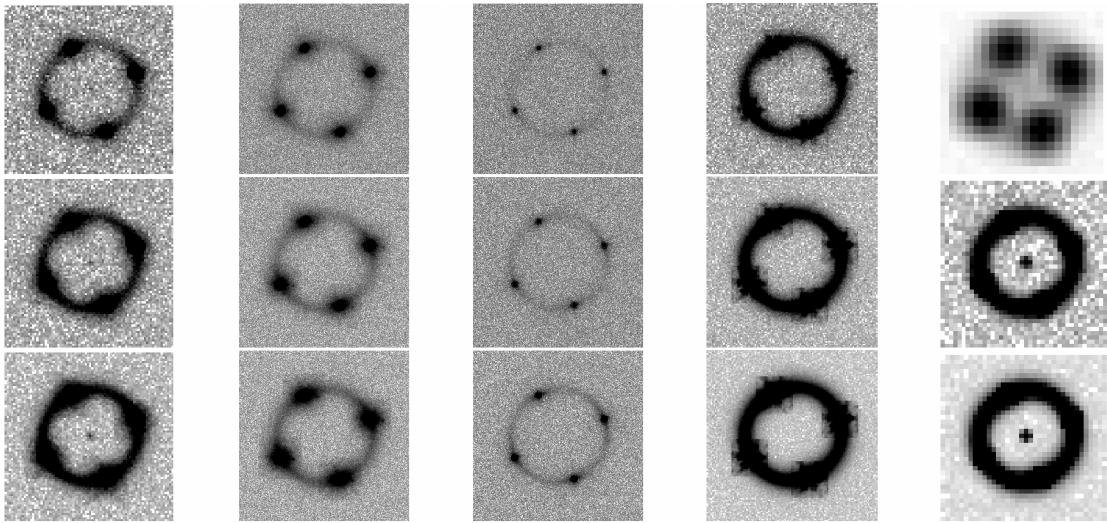


Figure 5. Same as Fig. 4, for the bright quadruply imaged system. **XLM to remake figure after masking black spot artifacts at the center.**

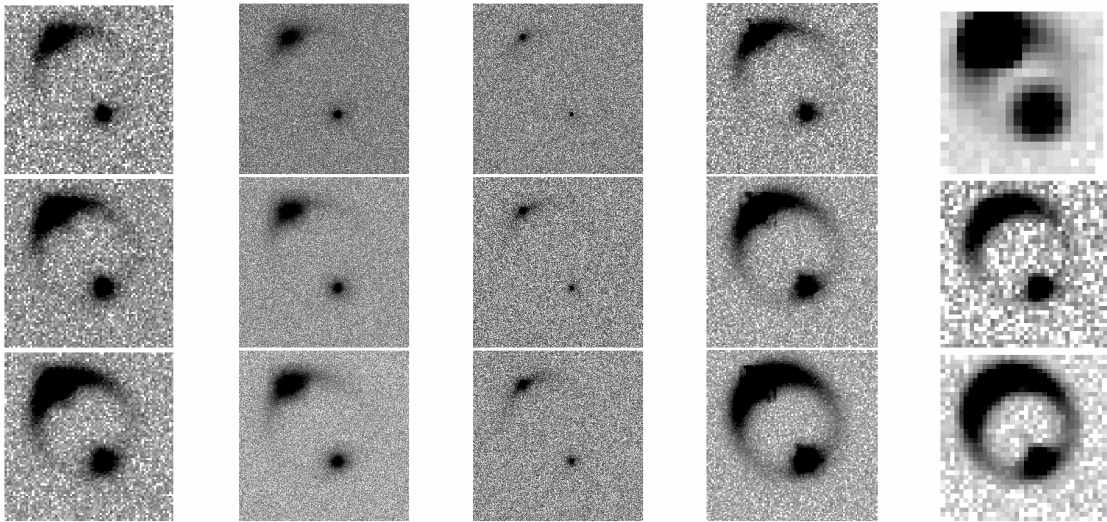


Figure 6. Simulations of the bright lens system with 2 QSO images. The simulated images are all $4'' \times 4''$. The first 3 columns, from left to right, represent HST/ACS, Keck/NIRC2+LGSAO, Keck/NIRC2+NGAO; from top to bottom, the rows correspond to $1/3 \times$ "target" exposure time, "target" exposure time, and $3 \times$ "target" exposure time. "Target" exposure time is defined as the exposure time that yields 2% precision on the slope of the mass density profile of the mass model γ' . The fourth column shows JWST simulations with 3 fixed exposure times: 60, 180, 540 seconds, from top to bottom. The fifth column shows simulations of 3 surveys. From top to bottom we show LSST, Euclid, and WFIRST, with the default survey exposure times (4500s, 2360s, 920s, respectively). TMT simulations are not shown since the system is considered too bright to be observed with this telescope in practice.

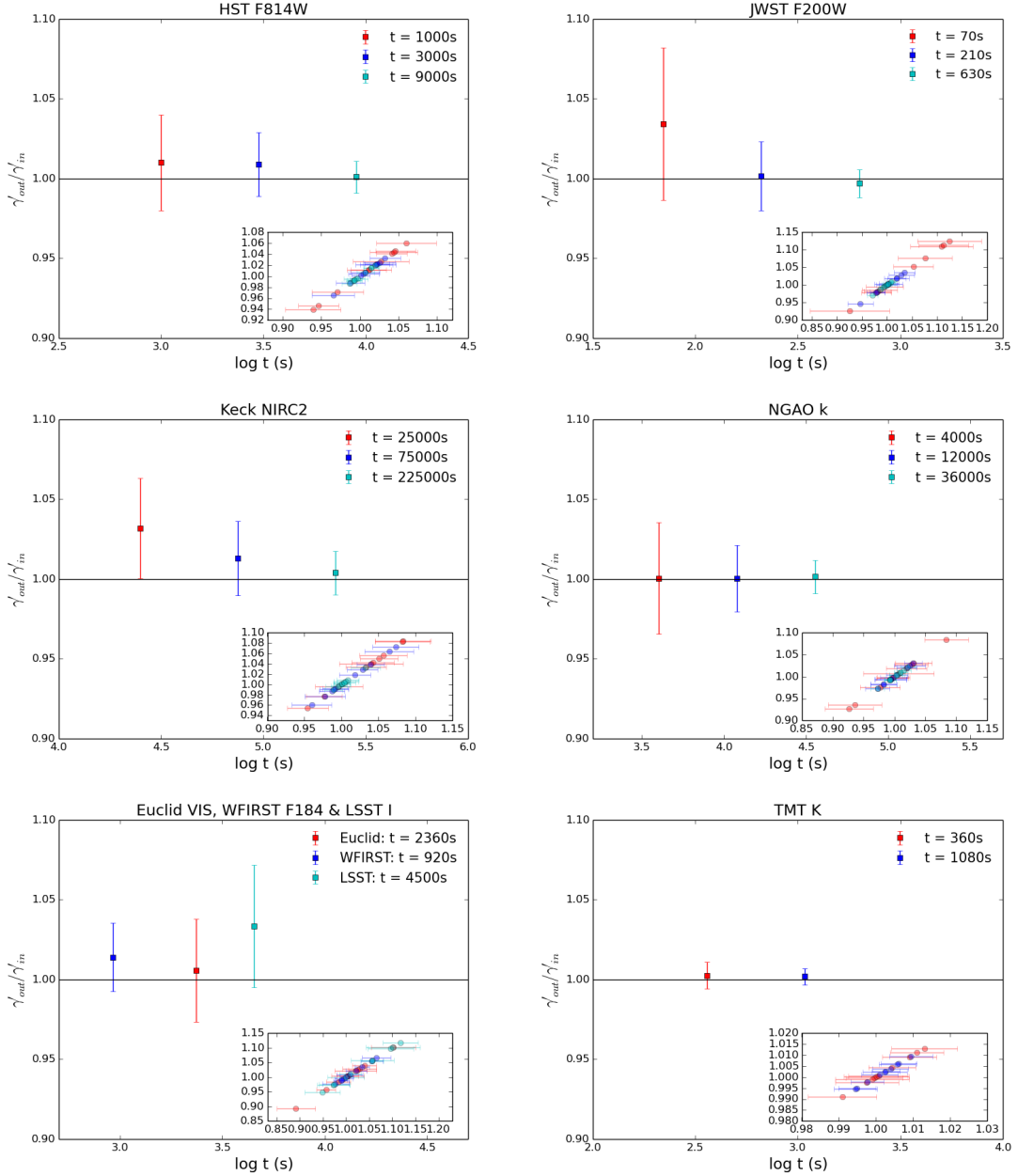


Figure 7. Precision on the mass density profile slope γ' as a function of exposure time. This figure shows the results for the fainter lens system with 4 QSO images. The quantity γ'_{in} is the input SIE mass slope. The quantity γ'_{out} is the output of the inference process. The insert in each panel shows all 10 simulation results for each exposure time with the same color coding. Note that both axes represent $\gamma'_{out}/\gamma'_{in}$ whereas error bars are only shown on the x-axis for clarity.

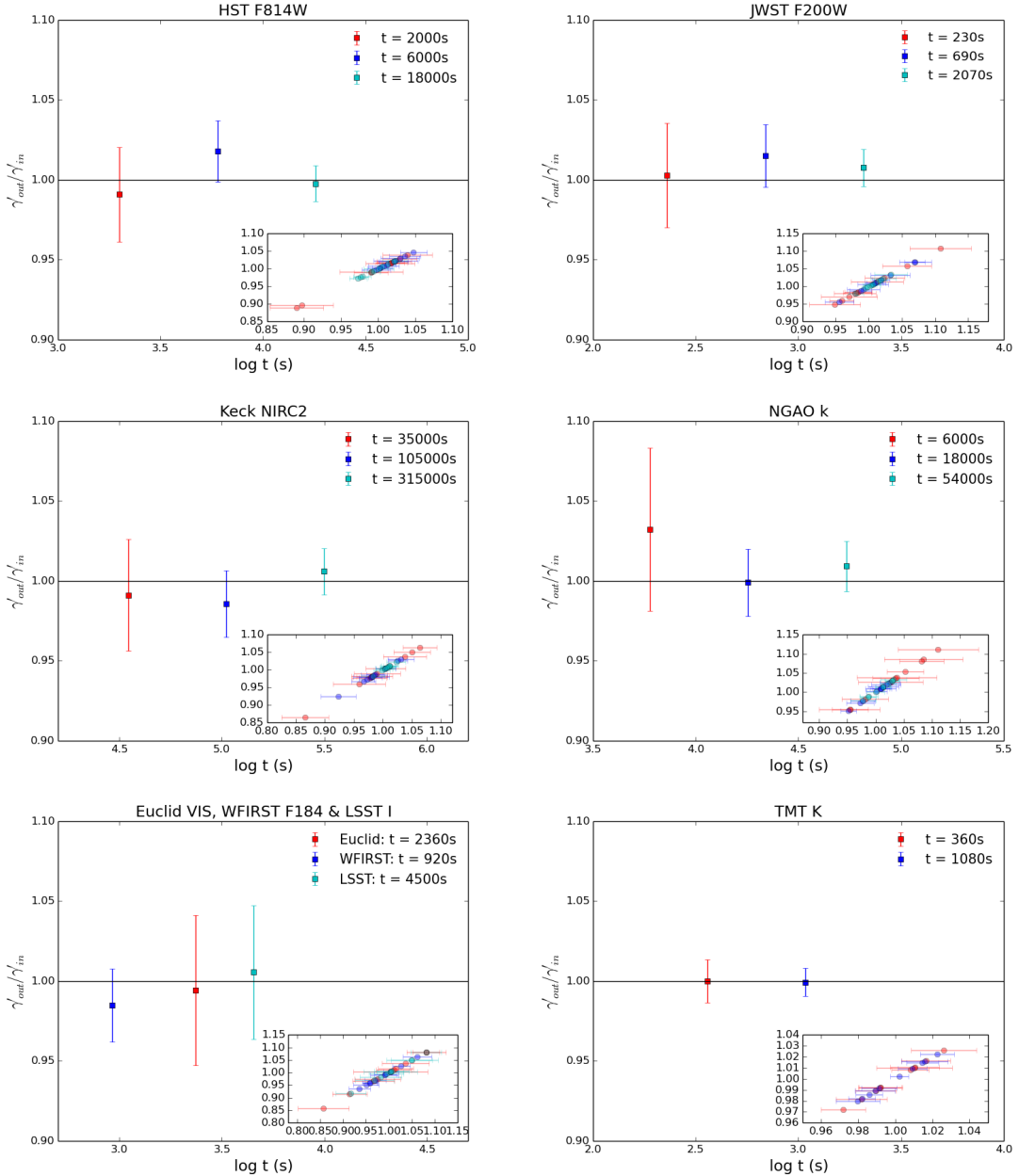


Figure 8. Same as Fig. 7 for the fainter lens system with 2 images.

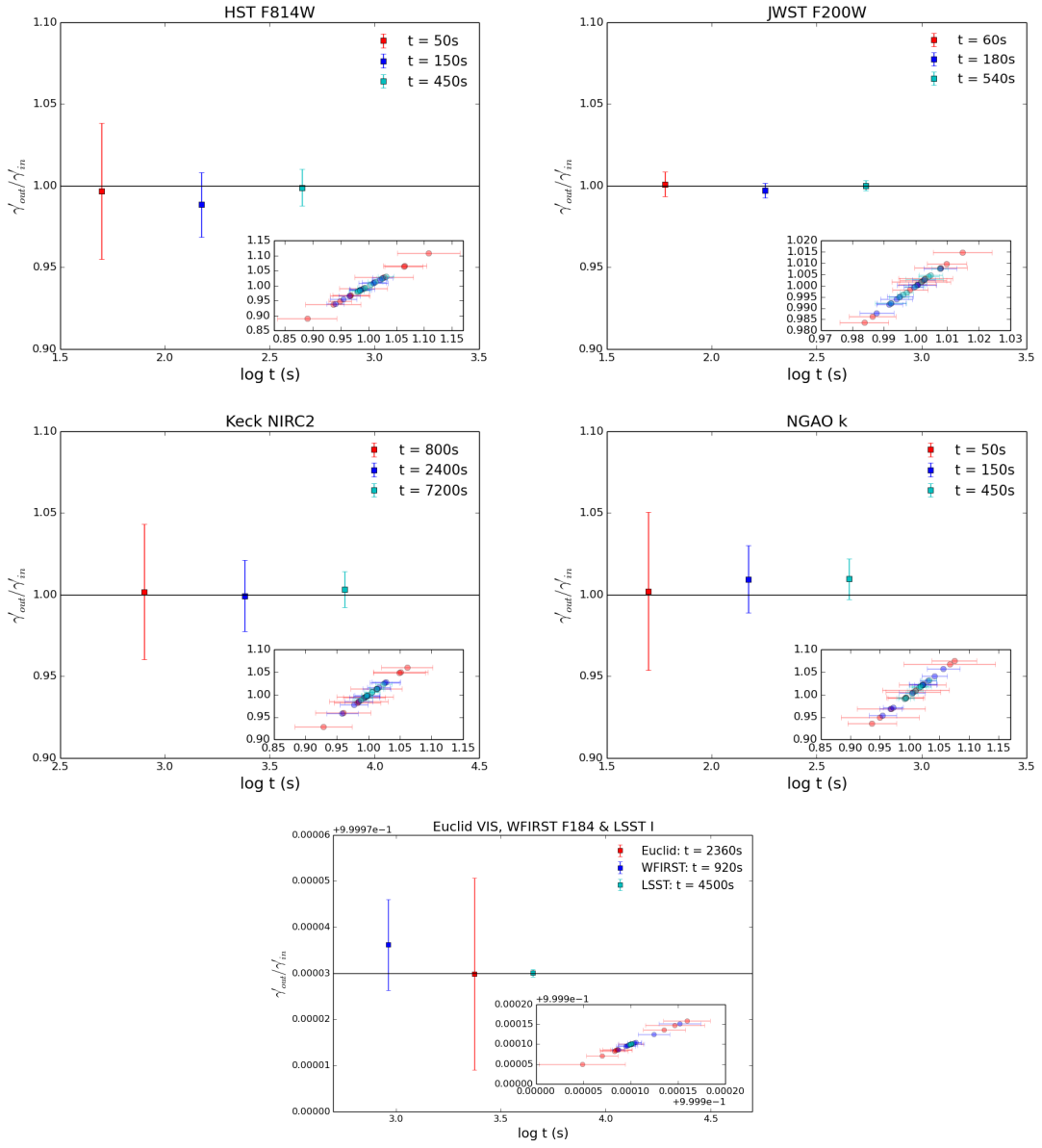


Figure 9. Same as Fig. 7 for the brighter lens system with 4 images.

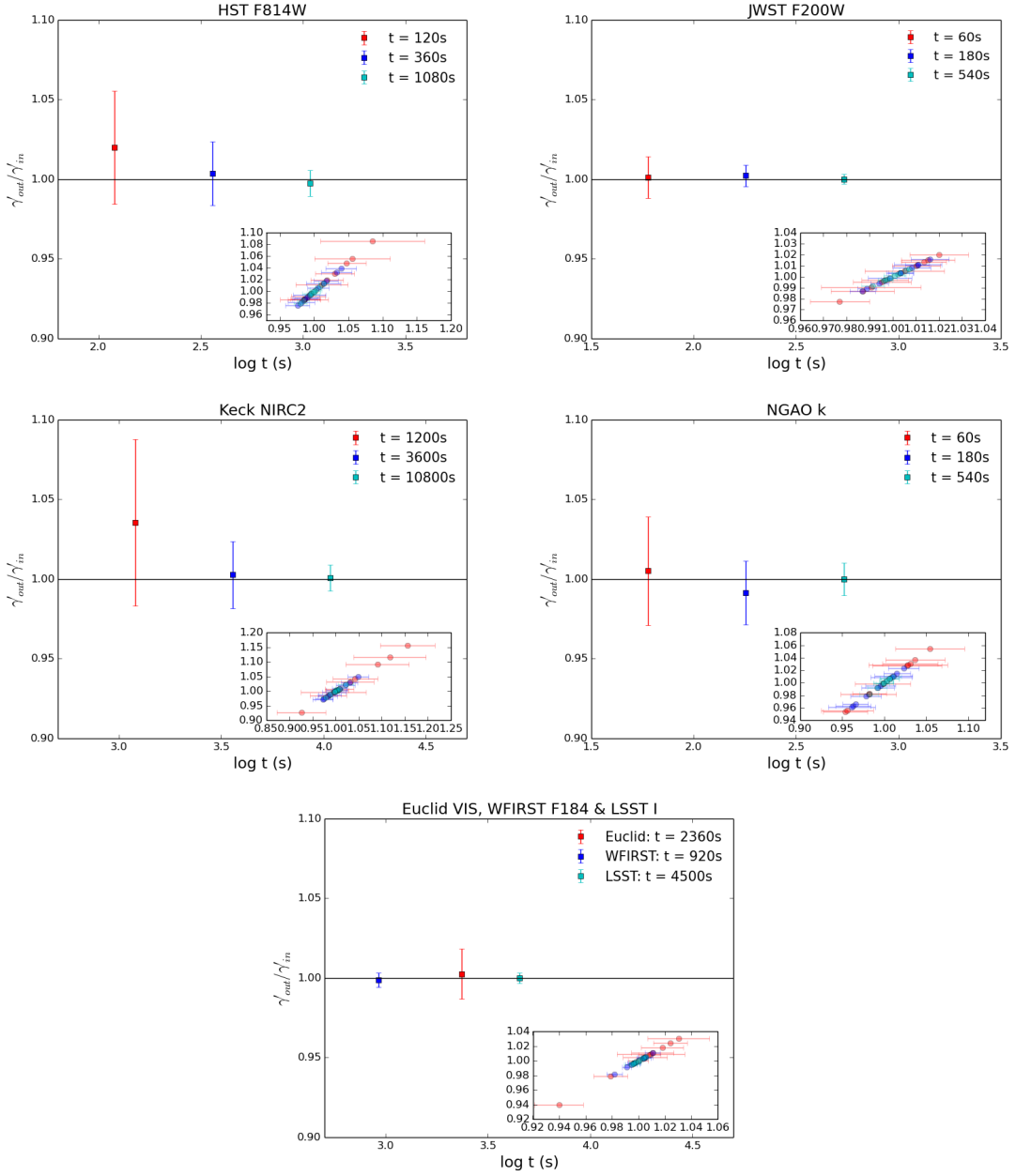


Figure 10. Same as Fig. 7 for the brighter lens system with 2 images.